Article

The International Journal of Robotics Research
1–18

DOI: 10.1177/0278364920935514
journals.sagepub.com/home/ijr

An obstacle disturbance selection framework: emergent robot steady states under repeated collisions

Feifei Qian and Daniel E Koditschek

Abstract

Natural environments are often filled with obstacles and disturbances. Traditional navigation and planning approaches normally depend on finding a traversable "free space" for robots to avoid unexpected contact or collision. We hypothesize that with a better understanding of the robot–obstacle interactions, these collisions and disturbances can be exploited as opportunities to improve robot locomotion in complex environments. In this article, we propose a novel obstacle disturbance selection (ODS) framework with the aim of allowing robots to actively select disturbances to achieve environment-aided locomotion. Using an empirically characterized relationship between leg–obstacle contact position and robot trajectory deviation, we simplify the representation of the obstacle-filled physical environment to a horizontal-plane disturbance force field. We then treat each robot leg as a "disturbance force selector" for prediction of obstacle-modulated robot dynamics. Combining the two representations provides analytical insights into the effects of gaits on legged traversal in cluttered environments. We illustrate the predictive power of the ODS framework by studying the horizontal-plane dynamics of a quadrupedal robot traversing an array of evenly-spaced cylindrical obstacles with both bounding and trotting gaits. Experiments corroborate numerical simulations that reveal the emergence of a stable equilibrium orientation in the face of repeated obstacle disturbances. The ODS reduction yields closed-form analytical predictions of the equilibrium position for different robot body aspect ratios, gait patterns, and obstacle spacings. We conclude with speculative remarks bearing on the prospects for novel ODS-based gait control schemes for shaping robot navigation in perturbation-rich environments.

Keywords

Legged robots, locomotion, obstacle interaction, cluttered environment

1. Introduction

Existing research on robot navigation and path planning (Khatib, 1986; LaValle, 2006) has largely been premised on a clear distinction between a traversable ''free space,'' separated from the set of ''obstacles'' that can never be even touched. Indeed, because most available platforms lack any capability to cope with unanticipated mechanical contacts, robots generally rely heavily on active sensing to avoid engagement of any kind. However, as our increasingly capable robots begin to operate in more natural, less structured environments, it seems clear that this constraint must be relaxed, or even exploited.

We hypothesize that the disturbances from obstacles can be regarded as opportunities to enhance mobility in complex environments (Figure 1). Biological studies have demonstrated that animals (Kinsey and McBrayer, 2018; Kohlsdorf and Biewener, 2006; McInroe et al., 2016; Wilshin et al., 2017) can coordinate their appendages or body segments (Schiebel et al., 2019; Zhong et al., 2018) to adjust the timing and positions of environment engagement (Gart and Li, 2018; Gart et al., 2018; Li et al., 2015) to achieve effective locomotion. In analogy to the selected leg sequence timing in biological locomotors, Johnson and Koditschek (2013) demonstrated that with a human-programmed leg activation sequence, a hexapedal robot can jump up a vertical cliff by using its front legs to hook

Department of Electrical and Systems Engineering, University of Pennsylvania, Philadelphia, PA, USA

Corresponding author:
Feifei Qian, Ming Hsieh Department of Electrical and Computer Engineering, University of Southern California, 3740 McClintock Ave, Los Angeles, CA 90089, USA.
Email: feifeiqi@usc.edu

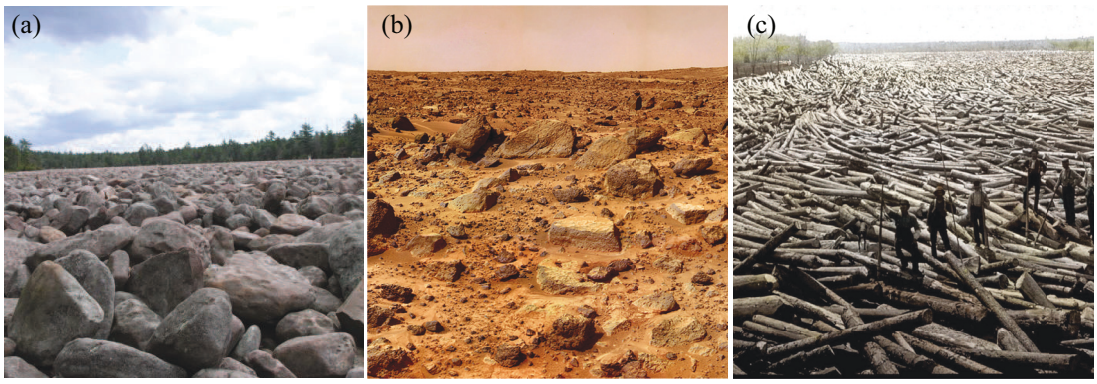

Fig. 1. Natural terrains on Earth and in extraterrestrial environments are often filled with obstacles that generate large, repeated disturbances to robot locomotion. (A) Boulder field at Hickory Run State Park. Photo courtesy of Clyde. (B) Martian surface. Photo taken by NASA's Curiosity Rover. (C) Log jam. Photo courtesy of Scampblog.

on the cliff edge while pushing its rear legs against the vertical surface. These studies suggested that with a better understanding of environment responses and interaction dynamics, robots could exploit obstacles and collisions to achieve environment-aided locomotion.

A key challenge in endowing robots with the ability to autonomously generate such environment-aided locomotion is the problem of conceptualizing how to even extract information about, much less exploit, these interaction opportunities from physical properties (e.g., shape, size, distribution) of the environment. On flat and rigid ground, robot dynamics can be modeled accurately (Blickhan, 1989; Brown and Loeb, 2000; Schmitt and Holmes, 2000), and numerous methods have been developed for control and planning on such simple terrain (De and Koditschek, 2018; Raibert, 1986). However, once the robots are allowed to interact with more complex environment (Li et al., 2010; Marvi et al., 2014; Qian and Goldman, 2015b; Qian et al., 2013), many simplified models and templates (Full and Koditschek, 1999) fail to capture the coupled dynamics, and previous control and planning methods are no longer applicable.

Gibson (1979) proposed the notion of environmental affordance as an agent's acting to exploit an environmental structure in a manner favorable to some desired outcome. In the past few decades, there have been a number of biomechanics (Gart et al., 2019; Li et al., 2015; McInroe et al., 2016; Sane and Dickinson, 2001; Schiebel et al., 2019; Winter et al., 2012) and robotics (Arslan and Saranli, 2012; Bayraktaroglu and Blazevic, 2005; Byl and Tedrake, 2009; Curet et al., 2010; Kim et al., 2008; Qian and Goldman, 2015a; Qian et al., 2013; Rieser et al., 2019; Transeth et al., 2008; Winter et al., 2014) studies that began to reveal a wide variety of environmental affordances (Gibson, 1979) for locomotion, and how different locomotor morphology and kinematics allows exploitation of such affordances to effectively move through complex environments.

As a first step towards constructing a general framework of exploiting environmental affordance through gaits (Gibson, 1979), in this study we abstract the physical obstacles to treat them as the source of a horizontal-plane disturbance force field (Section 3.1). A previous study (Qian and Goldman, 2015b) on robot interaction with a single obstacle revealed that the change of robot orientation state after the interaction depended primarily on the initial fore–aft contact position on the obstacle. In this work, we expand this empirically characterized relationship to propose a disturbance field representation of horizontal-plane obstacle influences on robot dynamics. The values of the two-degree-of-freedom (2-DoF) disturbance field represent the direction and magnitude of fore–aft obstacle forces on the hip joint of a contacting robot leg.

The disturbance field provides a map of available interaction forces in the given physical environment. That said, the total obstacle reaction forces on and the resulting dynamics of the center of mass (CoM) of a robot depend sensitively on the position and time of contact between robot legs and obstacles. In this article, we regard robot legs as a collection of disturbance selectors (Section 3.2), and we calculate the total interaction force exerted on the robot CoM by adding disturbance forces from each leg in contact with the obstacle. By coordinating leg movements and engaging its limbs with obstacles at different positions and times, a multi-legged robot can elicit a wide variety of dynamical effects from the same environment.

Combining the disturbance-field representation of environment and the disturbance-selector representation of the locomotor, our obstacle disturbance selection (ODS) framework provides a general method to predict robot dynamics under obstacle modulation. To validate our method, we construct a numerical model (Section 4) using the ODS framework. We study in both experiment (Section 2) and numerical simulation (Section 4) the dynamics of a quadrupedal robot, HQ-RHex (Figure 2A,

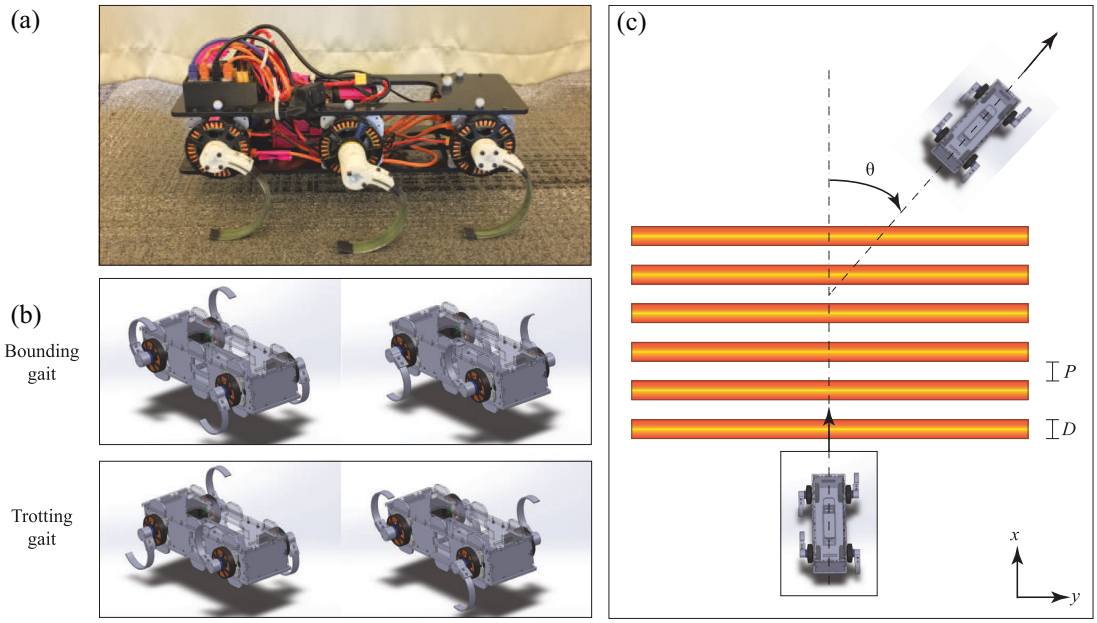

Fig. 2. Experiment setup for exploring the effect of different gaits on robot traversal of a periodic obstacle field. (A) HQ-RHex, a small RHex-class (Saranli et al., 2001) robot. For experiments in this study we used a quadrupedal version of this robot by removing the two middle legs. (B) Two quadrupedal gaits were tested in the experiment, both of which involved two sets of two legs paired in phase, with the two pairs of legs in anti-phase. In bounding, two front legs are paired to move synchronously and then alternate with the two back legs; in trotting, two diagonal legs are paired and alternates with the other pair. (C) HQ-RHex's instantaneous CoM positions (x, fore–aft; y, lateral; z, vertical) and orientations (pitch; yaw; θ, roll) were recorded as it traversed over an array of evenly spaced half-cylindrical obstacles.

Section 2.2), as it locomotes across an array of half-cylindrical obstacles (''logs''). Although a quadruped, a relatively simple form of multi-legged platform, is used to demonstrate the application of our framework in experiment (Section 2) and simulation (Section 4), we posit that the framework described in Section 3 is applicable to more general multi-legged platforms with different numbers of legs.

We analyze the horizontal-plane dynamics of the HQ-RHex robot for two periodic gaits, a bound and a trot (Figure 2B). In both experiments and ODS-framework-derived numerical simulation, we find that the bounding robot exhibits a stable equilibrium state at a yaw angle of 0° independent of initial orientation or obstacle spacing, whereas the trotting robot exhibits orientation equilibria at $\pm\theta°$, with $\theta \in (0°, 90°)$ independent of initial orientation but dependent on obstacle spacing and robot aspect ratio.

Further analysis suggests that the emergence of this ''locking angle'' is a result of spatial period matching (Section 5) between the cyclic gait and the periodically structured environment. Using the spatial period matching principle, we demonstrate that the equilibrium orientation angle can be analytically predicted for a variety of obstacle spacings and robot body dimensions. In addition, the emergence of this passive stabilization mechanism from the simplified environments (periodic gaits in structured obstacle fields) suggests the possibility of active gait control schemes in more complex environments. We envision that by actively adapting gait sequences, a multi-legged robot can strategically select obstacle disturbances to achieve desired dynamics in cluttered environments (Section 6).

2. Obstacle modulation experiments

To begin to understand how robot dynamics changes under repeated obstacle disturbances, we performed locomotion experiments with a quadrupedal robot traversing across a field of evenly spaced obstacles. We systematically varied obstacle spacing and robot gait, and analyzed how these parameters affect the coupling between the robot and the environment.

2.1. Environment

The environment we used in this study was a simplified obstacle field with an array of half-cylindrical obstacles (''logs'') of diameter D and spacing P (Figure 2C). The periodic structure reduces the uncertainty in repeated obstacle disturbances, and allows the observed stable interaction pattern to emerge (see Section 2.4). The structured spacing also allows us to systematically vary P relative to the robot dimension and analyze how this parameter affects the stable interaction pattern (see Section 5.2). The symmetry of the cylindrical shape reduces the complexity

of modeling obstacle disturbance force fields (see Section 4.1). In addition, owing to the similar surface inclination profile between logs and spheres in the fore–aft direction, we are able to use the empirical results from Qian and Goldman (2015b) to generate the disturbance force field in this study.

The outer diameter D of the half-cylindrical obstacles was chosen to be ≈0.11m, comparable to the robot leg size (0.12m outer diameter) so that the each obstacle interaction would produce a significant amount of perturbation to the robot locomotion but would not cause the robot to get stuck or flip over. Obstacle spacing P was chosen to be ≈0.10m, slightly smaller than the step length (0.15–0.2m on flat ground) of the robot, such that the robot would be repeatedly disturbed during every step but would not be able to return to its flat-ground steady state between disturbances.

2.2.Robot

The robot used in this study, HQ-RHex (48cm in length, 27cm in width, 4.8kg, Figure 2A), is a RHex-class (Saranli et al., 2001) robot with six C-shaped legs. The robot body was made with laser-cut ABS plastic to allow quick morphological parameter variations for laboratory experiments. The legs were actuated by gearless direct-drive motors (Tiger Motor, U8) to achieve better force transparency (Kenneally et al., 2016) during interaction with obstacles. The legs were made from a relatively rigid material, 14-ply composite fiber glass (Custom Composite Technologies Inc.), to reduce deformation during obstacle collision and facilitate contact modeling. The outer sides of the legs were coated with 2mm thick rubber to increase traction on flat ground. The robot was powered by a four-cell Li-Po battery (16.8V when fully charged), and battery voltage was monitored between experiments and maintained at a minimum of 16V for all trials. The gait and clock parameters (Saranli et al., 2001) and the stride frequency of the robot were controlled by a customized (Kenneally et al., 2016) micro-controller (Ghost Robotics MBLC v0.5.2).

As a first step to investigate the effect of gait patterns on robot dynamics under obstacle modulation, we tested the dynamics of HQ-RHex with two periodic gaits, bounding and trotting (Figure 2B). Bounding refers to the gait where two front legs move synchronously and two back legs move synchronously and out of phase with the front legs. Trotting refers to the gait where two diagonal legs move synchronously and out of phase with the other two legs.

2.3. Data collection and analysis

We performed 49 experiments with a bounding gait and 68 experiments with a trotting gait. We selected the initial fore–aft distance to ensure that the robot maintains the desired initial orientation and moves at least three complete stride cycles before entering the obstacle field. Each bounding trial started with the robot standing with a fore–aft distance of $\sim 1.2 \pm 0.1$ m in front of the first obstacle, with desired initial orientation angle between 0° and 60° with an increment of 5°. For initial orientation angles larger than 60°, the robot deflected off the first log and failed to enter the obstacle field in most of the trials. We performed three trials for each desired initial orientation angle. We only performed trials with positive initial orientation angle owing to the symmetry. Similarly, each trotting trial started with the robot standing with a fore–aft distance of $\sim 1.0 \pm 0.2$ m from the first obstacle, with desired initial orientation angle between 0° and 60° with an increment of 5° on both sides. We performed five trials for each positive initial orientation angle. Owing to symmetry, we performed fewer trials for negative initial orientation (one trial per initial orientation angle).

We used a wireless remote joystick (Quanum i8) to set the stride frequency and gait pattern of the robot at the beginning of each trial. Once the trial started, the leg motors followed a desired angular position sequence generated based on the commanded stride frequency and gait pattern, and the robot traversed the obstacle-cluttered terrain in a feed-forward fashion without steering control. All changes in robot orientation, therefore, resulted from obstacle disturbances.

For each trial, the robot was set to a fixed stride frequency. Two different stride frequencies, 0.5 and 2Hz, were tested. For the equilibrium steady states discussed in this article, there is no major difference between the two different stride frequencies. We merge the results from different stride frequencies in later discussions. During each stride, the instantaneous angular position of each leg was specified by the ''Buehler clock'' parameterization of stance and flight phasing as described in Saranli et al. (2001). For all trials in this study, the angular extent of the stance phase was set to 60° with its center at −15°. Leg angles are measured clockwise about the axle and between the downward vertical and a diameter through the axle. The fraction of time spent in stance during each leg rotation (duty cycle) was set to 70%.

To track the dynamics of the robot during interaction with obstacles, we glued reflective markers (B&L Engineering, 12.7mm) to the robot and tracked its CoM positions (x, fore–aft; y, lateral; z, vertical; Figure 2C) and orientations[1] (pitch, yaw, roll) using a 20-camera motion capture (Vicon) system. In this experiment, all obstacles were fixed on the ground and not allowed to move during the interaction. We attached tracking markers on each obstacle to record their actual positions. In addition, the robot gait parameters, leg positions, motor torques, and inertial measurements (measured by IMU VectorNav 100-S) were logged to an onboard SD card on the robot controller to complement Vicon measurements.

The initial orientation angle of the robot before it began interacting with the obstacle field, θ_0, was calculated as the average yaw angle of the robot CoM, before either of

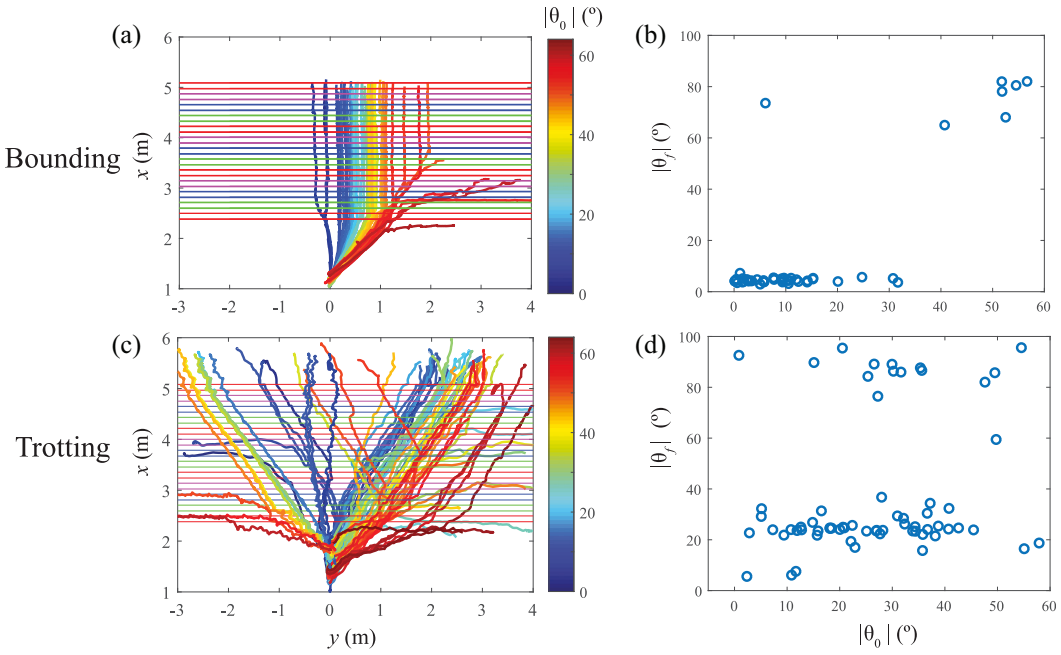

Fig. 3. Robot trajectories and steady-state yaw angles measured from experiments. (A) Paths of the robot traversing across the obstacle field with a bounding gait. Colors represent different initial yaw angle magnitude. Horizontal lines represent the obstacles' positions. Each obstacle was marked by a distinct color, with two horizontal lines representing the front and back edges. (B) Magnitude of the final yaw angle θ_f for different magnitude of initial yaw angle θ_0 in bounding experiments. Each circle represents one trial. (C) Paths of the robot traversing across the obstacle field with a trotting gait. Color convention is the same as (A). (D) Magnitude of final yaw angle θ_f for different magnitude of initial yaw angle θ_0 in trotting experiments. Each circle represents one trial.

the front legs reached the front edge of the first log. Similarly, to obtain the final orientation angle after the robot reached a steady state in the obstacle field, θ_f, average CoM yaw angle was calculated for the last 0.5m of trajectory before either of the robot front legs exited the obstacle range.

2.4.Experiment observations

Robot trajectories measured from experiments are plotted in Figure 3A and C. We observed that with a bounding gait, despite the large variation in initial orientations the robot converged to traversing perpendicularly across the logs ($\theta_f \approx 0$) after a few leg–obstacle collisions (Figures 3A and 4, and Extension 1), with the exception of a few trajectories with large initial orientation angles, where the robot converged to a trajectory that traverses sideways along the logs ($\theta_f = 90°$).

With the trotting gait, however, the stabilized orientations were significantly different from those with the bounding gait. None of the trajectories (Figure 3C) converged to $\theta_f = 0°$ as observed from the bounding gait experiments. Instead, the majority of the robot trajectories stabilized to a final orientation of $\theta_f = 24.7° \pm 4.2°$ (Figures 3C and 5, and Extension 2). For a few trajectories with small magnitude of initial yaw angle ($|\theta_0| < 15°$), the robot's final orientation does not stabilize to a fixed value, but oscillated periodically around $|\theta_f| = 5°$ (Figure 3C), much like a ''limit cycle''[2] behavior. Similar to the bounding gait case, the final orientation of the trotting robot could also stabilize at $\pm 90°$, in which case the robot traversed sideways.

Plots of $|\theta_f|$ (Figure 3B and D) supported our observation that 90° was a stable orientation state for both bounding and trotting gaits. In contrast, 0° was a stable orientation state for only the bounding gait (Figure 3B) and $\pm 25°$ was a stable orientation state for only the trotting gait (Figure 3D). That 90° was a stable orientation was not surprising, as when the robot traversed sideways ($\theta = 90°$) its legs could step on the flat ground between the logs, avoiding any obstacle disturbances that would push it away from the 90° orientation. If the robot slightly deviated away from 90° and one or more legs started to step on the edge of the logs, those legs would quickly slip off the edge of the logs and fall back to the gaps, and eventually bring the robot orientation back to around 90°. This is true for a variety of other gaits, and therefore 90° is a commonly observed steady state. Because the stability mechanism for 90° is trivial and is not significantly different for different gaits, we do not discuss this stable orientation further in the following sections. To investigate the mechanism behind the difference in stable orientation of 0° in bounding and $\pm 25°$ in trotting, in the following section (Section 3) we propose an ODS framework, where we model the robot gait as different timing patterns for robot legs to select obstacle disturbances.

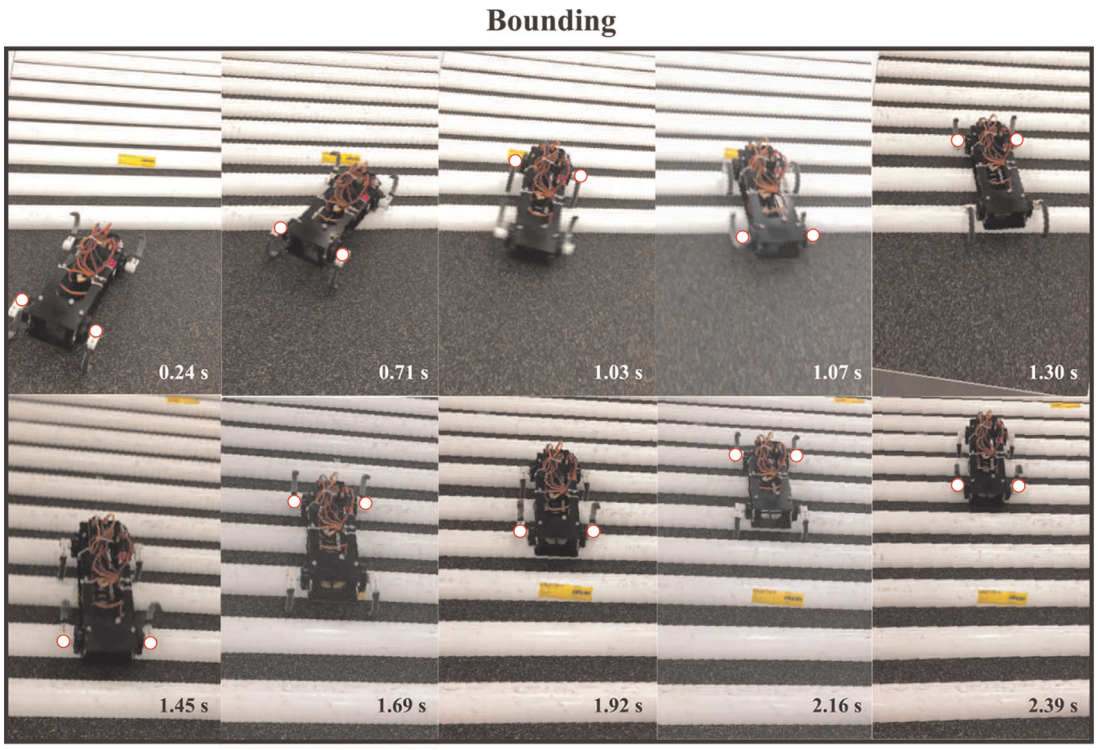

Fig. 4. Sequence of images from a bounding experiment showing the robot orientation was locked to 0° under periodic obstacle modulation. Circles highlight hips of the synchronized leg pair that was selecting obstacle disturbances.

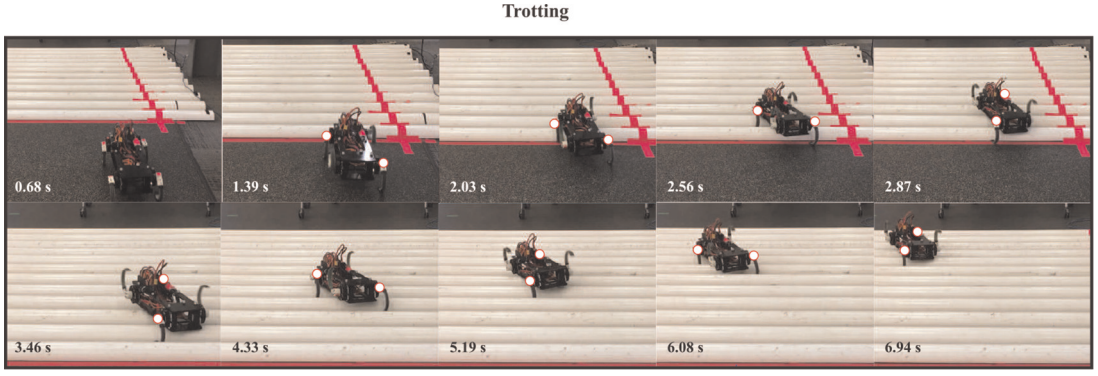

Fig. 5. Sequence of images from a trotting experiment showing the robot orientation was locked to -25° under periodic obstacle modulation. Circles highlight hips of the synchronized leg pair that was selecting obstacle disturbances.

3. ODS framework: connecting obstacle-modulated robot CoM dynamics to leg–obstacle contact positions

The surprisingly simple behavior of the obstacle-modulated robot steady state observed from experiments suggests that despite the complicated, repeated collisions between robot legs and obstacles, there exists a simple mechanism that dominates the obstacle-modulated robot CoM dynamics. In this section, we propose a horizontal plane ODS framework that abstracts and simplifies the complicated low-level contacts and explains the strikingly uniform steady-state robot orientation angles emerging from the leg–obstacle contacts.

The framework entails three key conceptual components, to generate a simplified representation of the environment, the gait, and the coupling between the two. The first component represents the physical obstacle perturbations as a simplified 2-DoF disturbance force field in the world frame (Section 3.1). The second component interprets the robot gait as an ‘‘activation pattern’’ whereby each activated leg selects the available obstacle disturbances at its location (Section 3.2). Selected disturbances from all activated legs contribute to the total external

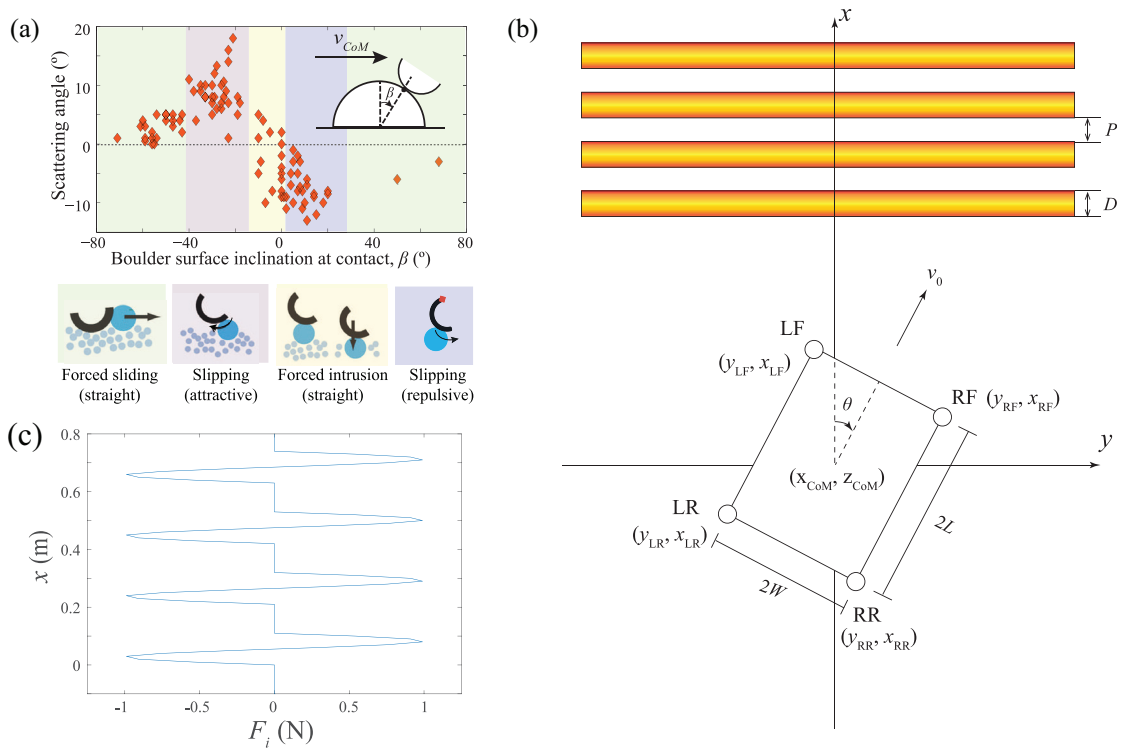

Fig. 6. Obstacle disturbance field model. (A) For SLSO interactions, robot orientation change (the ''scattering angle'') after the collision depends primarily on the fore–aft inclination angle, β, at the initial contact position (Qian and Goldman, 2015b). Here β is negative on uphill slopes and positive on downhill slopes. Scattering angle refers to the robot trajectory deviation after a single obstacle interaction. Positive scattering angle indicates attractive disturbance (i.e., the robot turns towards the obstacle after collision) and negative angle indicates repulsive disturbance (i.e, the robot turns away from the obstacle after collision). Reproduced from Qian and Goldman (2015b: Figure 5), where spherical mobile obstacle was used to demonstrate various leg–obstacle interaction modes. That said, it was discovered in Qian and Goldman (2015b) that the dependence of scattering angle on initial fore–aft contact position is similar between cylindrical fixed obstacle and spherical mobile obstacle (Qian and Goldman, 2015b: Figure 6). (B) Diagram of the repeated obstacle disturbances setup. Orange rectangles represent the array of cylindrical obstacles with diameter D and spacing P. The left front, right front, right rear, and left rear legs of the quadrupedal robot were represented as vertices LF, RF, RR, LR, respectively, of the rectangular box representing the robot body. The body length (distance between front and rear legs) is $2L$ and the body width (distance between left and right legs) is $2W$. The x axis represents the fore–aft direction in the world frame and the y axis represents the lateral direction in the world frame. Robot orientation, θ, is defined as the angle between x axis and robot heading. (C) Abstracted obstacle disturbance force field for evenly spaced cylindrical obstacles with $P = 0.10$m, $D = 0.11$m. Positive F_i indicates forward (i.e., $+x$ direction in B) disturbance force on leg i and negative F_i indicates backward (i.e., $-x$ direction in B) disturbance force on leg i.

forces and torques in the third component (Section 3.3), allowing calculation of the obstacle-modulated robot CoM state, $q := (x_{\mathrm{CoM}}, \theta)$, in the horizontal plane. Here x_{CoM} represents the fore–aft position of the robot's CoM in the world frame (x direction; Figure 2C), and θ represents the orientation angle of the robot's CoM body frame relative to the inertial world frame.

3.1. Obstacle abstraction and disturbance field generation

Qian and Goldman (2015b) found that the orientation of a legged robot could change up to $\pm 20°$ during one interaction event between one leg and one obstacle, depending on the initial condition of the leg–obstacle contact. It was also found that the direction and magnitude of the change in robot orientation (the ''scattering angle'' (Qian and Goldman, 2015b)) depended primarily on the fore–aft surface inclination angle on the obstacle, β (Figure 6A), at the initial contact position. This dependence was found for a variety of obstacle shapes and surface frictions in Qian and Goldman (2015b).

Here we use this dependence to convert physical obstacles into a 1-DoF artificial disturbance force field. In our ODS framework, we model each single-leg, single-obstacle (SLSO) collision as a disturbance force, f, exerted on the hip joint of the contacting robot leg. Since this disturbance primarily depends on the fore–aft obstacle surface inclination β for a given obstacle with known sagittal-plane shape profile, $\beta(\bar{x})$, we can use the universal disturbance–inclination relationship $f(\beta)$ (Figure 6A) (Qian and Goldman, 2015b) to obtain the obstacle

disturbance force (ODF) in the world frame, $f(\bar{x})$, as a function of $\bar{x}$. Here $\bar{x}$ denotes the relative contact position, the distance measured from the x-direction position of the contacting leg to the near edge of the contacting obstacle.

The total obstacle disturbance field comes from all obstacles in the physical environment. This 2-DoF ODF field that a robot leg (leg i) experiences, F_i, can be computed as a superposition of all localized SLSO responses, $f(\bar{x})$, based on the distribution of obstacles in the environment:

$$F_i = \begin{cases} f(\bar{x}_i) & (x_i, y_i) \in O \\ 0 & (x_i, y_i) \in G \end{cases} \quad (1)$$

Here x_i and y_i represent the fore–aft and lateral positions of leg i ($i \in H$, where H is the set of all legs $H = \{LF, RF, RR, LR\}$, Figure 6B) in the world frame, O represents the set of locations on the horizontal plane that is occupied by obstacles, and G represents the set of locations on the horizontal plane without obstacles. We note that in this highly simplified model we attach the disturbance obstacle force directly at the robot hip joint, and therefore do not take into account the periodic fore–aft oscillation movement of the leg relative to the hip joint.

Since F_i is a function of fore–aft positions in the world frame, Equation (1) provides an abstracted map of available obstacle reaction forces in the world frame. In the following sections, we show that combined with the simplified representation of robot gaits, a robot can use this map of available interaction forces to predict and plan obstacle-modulated CoM dynamics in cluttered environments.

3.2. Gait pattern abstraction and ODS

The obstacle disturbance force field provides the map of interaction force opportunities. To connect the repeated leg–obstacle collisions to the change of robot state, we represent each robot leg as a ''disturbance selector''. At each instant, two conditions are necessary for a leg i to ''select'' the obstacle disturbance at its current location. First, leg i must be within the obstacle portion of the space, O (as opposed to the flat ground portion, G), see Equation (1). Second, leg i must be in stance phase.

The second condition provides a multi-legged robot the option to select different combinations of obstacle disturbances. To study the effect of such selection, we model robot gaits as a time-varying ''activation pattern'', $S(t)$. At any instance in time, S represents the subset of robot legs that are in stance phase ($S : \mathbb{R} \to \mathcal{P}(H)$)[3], and therefore subject to ground reaction forces and obstacle disturbances. The total force exerted on the robot CoM, F_o, can then be calculated for the specific gait as a sum of the ODF from all contacting legs:

$$F_o = \sum_{i \in S(t)} F_i \quad (2)$$

Similarly, the total torque exerted on the robot CoM by the obstacles can be calculated as

$$T_o = \sum_{i \in S(t)} (F_i \Delta y_i) \quad (3)$$

where y_i is the lateral position of leg i, and $\Delta y_i = y_i - y_{\mathrm{CoM}}$ is the relative lateral position of leg i relative to the CoM, both in the world frame.

We note that the ODS framework presented in this section applies not only to the quadruped demonstrated in Section 4 but also more general multi-legged platforms.

As Equations (2) and (3) stipulate, the obstacle disturbances for multi-leg, multi-obstacle (MLMO) situations depend on both the environment properties (the obstacle disturbance force field) and the choice of gait patterns. Given the same physical environment (i.e., same obstacle disturbance field), the total perturbation to the robot CoM can be significantly different depending on the activated leg groups (i.e., subset of legs) or their sequencing. Therefore, by using a different gait pattern or designing a different leg group sequence (such as a transitional gait), a legged robot can select over a highly diverse range of influences over a fixed terrain (see Section 6).

3.3. Robot CoM dynamics under obstacle disturbance modulation

Combining the disturbance field representation of the leg–environment interaction and the disturbance selection pattern representation of robot gait yields an abstraction of the robot CoM dynamics in response to repeated obstacle collisions.

On flat ground, the robot does not experience obstacle disturbances, and the CoM's fore–aft acceleration is determined by the thrust force, F_{th}, propelling the robot along the current orientation, in opposition to the stabilizing damping force, F_d. Both thrust force and damping force are defined in the local robot frame (F_{th_r}, F_{d_r}) and projected to the world frame (F_{th_w}, F_{d_w}) to calculate CoM acceleration along the x direction. Once engaged, the obstacle's perturbing influence is represented by the additional force term, F_o (Equation (2)), defined in the world frame. These three forces together yield the robot's fore–aft acceleration in the world frame, given by

$$\ddot{x}_{\mathrm{CoM}} = \frac{1}{m}(F_{ow} + F_{\mathrm{th}w} + F_{dw}) \quad (4)$$

where m is the mass of the robot.

Similarly, our ODS abstraction neglects the small oscillations in orientation due to each step on flat ground while positing an obstacle-engaged disturbance torque, T_o (Equation (3)), opposed by a stabilizing damping term, T_d, which allows the robot to subsequently recover a steady orientation:

$$\ddot{\theta} = \frac{1}{I}(T_o + T_d) \tag{5}$$

where I is the moment of inertia of the robot.

4. Numerical model: capturing robot steady states under periodic obstacle modulation using the ODS framework

In this section, we demonstrate how the obstacle-modulated robot states can be computed using the ODS framework, and we use the results to explain the emergence of the robot's steady states observed in experiments.

We implemented a numerical model in MATLAB Simulink to compute robot state under repeated obstacle perturbation. To facilitate comparison with experiments, in the numerical study we used the same setup as the experiment, with a quadrupedal robot traversing over evenly spaced cylindrical obstacles, and we compared the behaviors of the bounding and trotting gaits. All dimensions used in the simulation were directly measured from the experiments.

The numerical model executes three steps corresponding to the three components in the ODS framework. The first step (Section 4.1) computes the disturbance force field in the world frame based on the distribution of the obstacles in the physical environment. The second step (Section 4.2) generates a time series of leg activation set based on the two given gait patterns (Equations (12) and (13)), and computes the total disturbance force and torque exerted on the robot CoM. The third step (Section 4.3) updates the time-varying robot CoM state (fore–aft position x_{CoM} and orientation angle θ) in the world frame by numerically integrating the equation of motion under obstacle modulation in discrete time steps.

In Section 4.4, we show that the highly simplified horizontal-plane model is able to successfully capture the equilibrium steady-state behaviors of the coupled robot–obstacle system observed from experiments for both bounding and trotting gaits. In addition, the framework allows examination of forces and torques exerted on robot legs and CoM that lead to the observed steady states, and therefore facilitates discovery of the underlying mechanism of obstacle modulation behind seemingly complicated repeated leg–obstacle collisions.

4.1. Obstacle abstraction

Based on the ODS framework, each obstacle is modeled as a localized disturbance field, where the direction and magnitude of the disturbance force at each fore–aft position depends on the obstacle surface inclination. For the cylindrical obstacles (logs) used in our experiment, the SLSO disturbance $f(\bar{x})$ is the same as the spherical obstacles used in Qian and Goldman (2015b) owing to the same sagittal-plane shape profile. Therefore, in this article we use the empirically characterized relationship between robot trajectory deviation and fore–aft contact position for SLSO interaction from Qian and Goldman (2015b) to generate the ODF. We numerically approximate this previously empirically measured $f(\bar{x})$ as a sine function[4]:

$$f(\bar{x}_i) = \sin\left(\frac{2\pi\bar{x}_i}{D}\right) \tag{6}$$

This function qualitatively captures the dependence of obstacle disturbance observed in Qian and Goldman (2015b), where leg contacting on positive ($\bar{x}_i < D/2$) and negative ($\bar{x}_i > D/2$) obstacle inclination receives backward ($f(\bar{x}_i) < 0$) and forward ($f(\bar{x}_i) > 0$) disturbances, respectively, whereas contact position at zero obstacle inclination ($\bar{x}_i = D/2$) resembles flat ground and receives zero additional disturbance ($f(\bar{x}_i) = 0$).

As mentioned previously, $\bar{x}$ denotes the relative contact position, the distance from the x direction position of the contacting leg to the near edge of the contacting obstacle. For our experiment setting, $\bar{x}_i = mod(x_i, D+P)$[5] denotes the relative contact position of leg i. Here D is the log dimension, and P is the log spacing.

The fore–aft position of leg i in the world frame, x_i, depends on the robot's CoM state, $q := (x_{\mathrm{CoM}}, \theta)$ (Figure 6B):

$$x_{LF} = x_{\mathrm{CoM}} + L\cos(\theta) + W\sin(\theta) \tag{7}$$

$$x_{RF} = x_{\mathrm{CoM}} + L\cos(\theta) - W\sin(\theta) \tag{8}$$

$$x_{RR} = x_{\mathrm{CoM}} - L\cos(\theta) - W\sin(\theta) \tag{9}$$

$$x_{LR} = x_{\mathrm{CoM}} - L\cos(\theta) + W\sin(\theta) \tag{10}$$

In the experiments, obstacles were an array of evenly spaced logs along the y axis with diameter D and spacing P (Figure 6B). The obstacle distribution, therefore, is simply $O : [0, D)$ for the obstacle-occupied area, and $G : [D, D+P)$ for flat ground. For the low-frictional cylindrical obstacles with orientation along the y axis, the obstacle disturbance forces are mostly along the x direction. Given this lateral symmetry of the obstacle setup, the ODF field representing our experiment environment is 1-DoF (2-DoF in general cases). The 1-DoF obstacle disturbance field can be written as a periodic sine function with flat intervals (Figure 6C):

$$F_i(q) = \begin{cases} \sin\left(\frac{2\pi\bar{x}_i(q)}{D}\right) & \bar{x}_i(q) \in [0, \mathrm{D}) \\ 0 & \bar{x}_i(q) \in [\mathrm{D}, \mathrm{D}+\mathrm{P}) \end{cases} \tag{11}$$

Here F_i represents the available disturbance forces in the environment for any contacting leg. As mentioned in Section 3.1, F_i is a function of the x-direction positions in the world frame. Therefore, for a certain physical environment, the disturbance force field is fixed. However, as we will see in Section 4.2, for different gait choices, the total forces exerted on the robot CoM can be significantly different. By adjusting the timing and position of obstacle contact, a robot can potentially select desired environment

interaction forces to improve its locomotion and navigation in cluttered environments.

4.2. Disturbance selection

In a bounding gait, the two front legs always ''activate'' together to engage the obstacle disturbances at the same time, and then alternate with the two rear legs every half stride period, T. Therefore, we can write down the expression of the time-varying activation set, S, for a bounding gait:

$$S(t)=\begin{cases} LF, RF & 0 \leqslant t < T/2 \\ LR, RR & T/2 \leqslant t < T \end{cases} \tag{12}$$

We note that our model is highly simplified and not intended to take into account all physical details. In this highly simplified model, we assume perfectly alternating pairs. In physical experiments, the two pairs can overlap during stance depending on the duty cycle. Despite such simplification we show in Section 4.4 that the steady states persist.

Similarly, in a trotting gait, two diagonal legs always ''activate'' together and alternate with the other pair every half gait period. The activation set S for a trotting gait can therefore be written as

$$S(t)=\begin{cases} LF, RR & 0 \leqslant t < T/2 \\ RF, LR & T/2 \leqslant t < T \end{cases} \tag{13}$$

where T is the stride period, defined as the time takes for the robot to complete a stride cycle (two steps for both bounding and trotting).

With Equations (12) and (13), we can calculate the total obstacle disturbance force and torque on robot CoM using Equations (2) and (3):

$$F_o(q)=\sum_{i\in S(t)} F_i(q)$$

$$T_o(q)=\sum_{i\in S(t)} F_i(q)(y_i(q)-y_{\mathrm{CoM}}(q))$$

In this study, owing to the symmetry of the obstacles in the horizontal direction, the lateral position of the CoM was not updated.[6] Here y_i can be calculated as a function of the robot CoM orientation state, θ:

$$\begin{aligned} y_{LF} &= L\sin(\theta)-W\cos(\theta) \\ y_{RF} &= L\sin(\theta)+W\cos(\theta) \\ y_{RR} &= -L\sin(\theta)+W\cos(\theta) \\ y_{LR} &= -L\sin(\theta)-W\cos(\theta) \end{aligned}$$

Representing gaits as disturbance selection patterns allows a simplified analysis of how different S allows a robot to passively (i.e., without active steering) generate distinct horizontal-plane dynamics within the same environment.

4.3. State prediction

Here we compute the robot dynamics for different obstacle distributions and gait patterns using the total disturbance force and torque computed in the disturbance selection step (Section 4.2).

The fore–aft acceleration of the robot CoM in the world frame was calculated using the equation of motion (4). As mentioned in Section 3.3, on flat ground the robot's fore–aft acceleration is determined by the thrust force, $F_{\mathrm{th}r}$, and the damping force, F_{dr}, defined in the robot frame. Once engaged with obstacles, the obstacle disturbance force, F_{ow}, defined in the world frame, is added to the total force. In this study we are interested in capturing the robot steady-state orientation, which is insensitive to the thrust and damping force function forms, as suggested by the simulation data. Therefore, here we assume a constant thrust force, $F_{\mathrm{th}r}(q)=c_F$, in the robot frame. This thrust force is then projected onto the world frame as $F_{\mathrm{th}w}(q)=c_F\cos(\theta)$ to calculate the robot's acceleration along the x direction. The damping force, F_{dr}, scales linearly with the robot's fore–aft speed in the robot frame:

$$F_{dr}(q)=-c_x\dot{x}_{\mathrm{CoM}}$$

where c_F is the thrust force constant and c_x is the linear damping coefficient. Similarly, the damping force is projected to the world frame as $F_{dw}(q)=-c_x\dot{x}_{\mathrm{CoM}}\cos(\theta)$. Without obstacle modulation, the steady-state speed of the robot, v_{ss}, was determined by the values of the thrust force, F_{th}, and the linear damping coefficient, c_x. Here we use a thrust force constant, $c_F=2\mathrm{N}$, and a damping coefficient, $c_x=3$, yielding a resulting flat-ground speed of $v_{ss}(c_F,c_x)=0.6\mathrm{m/s}$, similar to the experimentally measured robot CoM speed for stride frequencies around 2Hz for both bounding and trotting gaits. The equilibrium position of robot orientation states were insensitive to the values of the constants, c_F and c_x.

The fore–aft position of the robot in the world frame, x_{CoM}, is then given by Equation (4):

$$\ddot{x}_{\mathrm{CoM}}(q)=\frac{1}{m}\Big(\sum_{i\in S(t)} F_i(q)+F_{\mathrm{th}w}(q)+F_{dw}(q)\Big) \tag{14}$$

In our simulation, x_{CoM} was updated at 0.01s using the ODE45 solver.

Similarly, the orientation of the robot, θ, was also updated at each time step. The change in the robot orientation was mainly driven by the total torque from obstacle disturbances, T_o. A damping torque proportional to the angular speed,

$$T_d(q)=-c_\theta\dot{\theta}$$

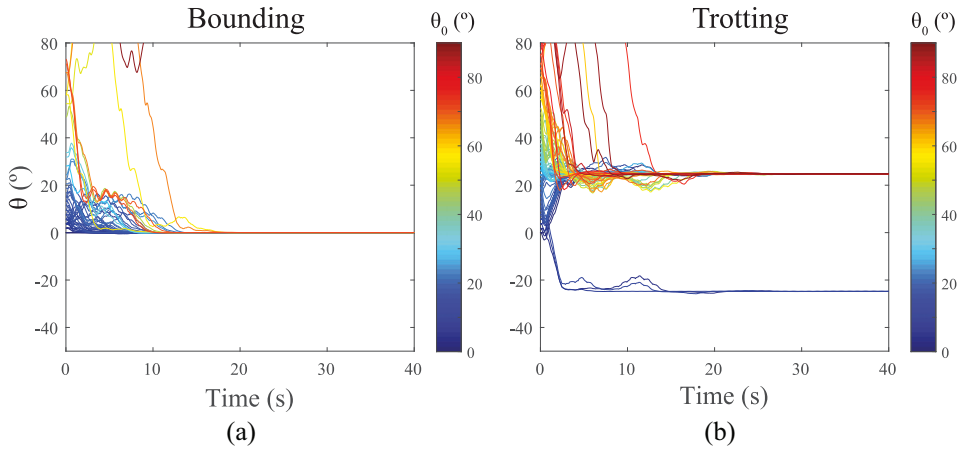

Fig. 7. ODS framework-based numerical simulation of robot orientation angle under repeated obstacle modulation (Equations (14) and (15)). Since limit cycles are beyond the scope of this article, only equilibrium trajectories with non-90° final orientations are plotted here. (A) Temporal trajectory of orientation of a bounding robot traversing over evenly spaced logs (Figure 6B) with spacing $P = 0.1$ m. Color represents initial orientation. (B) Temporal trajectory of orientation of a trotting robot traversing over evenly spaced logs with spacing $P = 0.1$ m. Color represents initial orientation.

was implemented to stabilize the robot after the perturbation:

$$\ddot{\theta}(q) = \frac{1}{I}\left(\sum_{i\in S(t)} F_i(q) y_i(q) + T_d(q)\right) \tag{15}$$

In our experiments, the weight of the robot, was primarily due to the battery (≈0.5 kg) at the CoM and the six motors (≈0.4 kg each) distributed at the edges and corners of the body, and therefore I, the moment of inertia of the robot, is calculated using a uniformly distributed weight assumption:

$$I = \frac{m[(2L)^2 + (2W)^2]}{12}$$

Here L is the model robot half body length (set to 0.178 m based on the experimentally measured distance between the front and rear legs), W is the model robot half body width (set to 0.127 m based on the experimentally measured distance between the left and right legs). We use c_θ to denote the angular damping coefficient. Simulation data show that the equilibrium state of the robot was insensitive to the variation of c_θ, but the convergence rate to steady states increased as c_θ increased. Here c_θ was set to 0.18 yielding a similar convergence rate as observed in experiments.

4.4. Capturing the observed steady states with the highly simplified ODS model

Here we calculate the robot steady-state orientation states for bounding and trotting using the numerical model. We compute robot state q for initial orientations between 0° and 90°, and initial fore–aft positions between 0 and environment spatial period, $P + D$. The final orientation angle, θ_f, is calculated by averaging the orientation angle θ for the last 10 seconds for trials where robot orientation stabilizes. We define the conditions for the equilibrium trials as: (1) the variation in orientation angle in the last 10 seconds is always smaller than 0.1°[7]; (2) the forward speed of the robot during the stabilized region is larger than 1 cm/s. The first criterion selects the trials where the robot stabilizes at a certain orientation angle or stabilizes at a limit cycle-like behavior with sufficiently small angular position oscillation range, whereas the second criterion eliminates trials where the robot is stuck in place.

Figure 7A and B show the robot orientation state computed from stabilized trials. Figure 7A demonstrates that similar to experiment observations, despite variations in initial conditions, a bounding robot has a steady-state orientation at 0°, where the robot moves stably along $+z$ direction (perpendicular to the logs) under repeated perturbation from the obstacles. Similarly, Figure 7B shows the robot orientation state for the trotting gait. Similar to experiment observations, a trotting robot can no longer maintain a steady-state orientation at 0° for the obstacle spacings tested, but would instead be attracted to one of the two stable equilibrium angular positions, $\pm\theta^*$. We show that we can analytically predict the equilibrium angular position θ^* for given log spacing and robot dimension in Section 5. Future work shall examine the interesting transient behaviors beyond equilibrium more closely.

5. Steady-state mechanism and prediction of equilibrium orientations using the ODS framework

The ODS framework not only allows numerically capturing the coupled dynamics, but since the computation of the change of states arises from physical understanding of low-level leg–obstacle interactions, the framework also

allows close examination of the forces and torques that lead to the steady states, and reveals the underlying mechanism that produces or maintains the equilibria of the coupled system.

In this section, we first discuss the mechanism for the emergence of the steady-state robot orientations observed in both simulation and experiments using the ODS framework (Section 5.1). We then use this discovered mechanism to develop a theoretical model (Section 5.2) to analytically calculate stable equilibrium states of robot orientation for different environments, robot morphology and gait parameters without requiring numerical simulation.

5.1. Mechanism of obstacle-modulated steady state

Here we calculate the equilibrium positions of the robot orientation using the ODS framework. The orientation state of the robot is $[\theta, \dot{\theta}]^{\mathrm{T}}$. From Equation (15) we know that at equilibrium orientation θ^* we have

$$\ddot{\theta}|_{\theta=\theta^*} = \frac{1}{I}\Big(\sum_{i\in S(t)}(F_i(t)y_i(t)) - c_\theta\dot{\theta}\Big)|_{(\theta,\dot{\theta})=(\theta^*,0)} = 0$$

which leads to the following condition at θ^*:

$$\sum_{i\in S(t)} T_o(q)|_{\theta=\theta^*} = \sum_{i\in S(t)}(F_i(q)y_i(q))|_{\theta=\theta^*} = 0 \qquad (16)$$

Intuitively, this means that the sum of torques from all contacting legs $i \in S(t)$ should remain zero at the equilibrium angle. For gaits such as bounding and trotting, one way to achieve this condition is for the two synchronously activated legs to always ''select'' canceling (i.e., same magnitude but opposite direction) obstacle disturbances to result in a total torque of zero.

5.1.1. Bounding analysis. For the bounding gait, the set of contacting legs S alternates between the two front legs, LF, RF, and the two rear legs, LR, RR. Therefore, the equilibrium orientation criterion in Equation (16) can be rewritten as

$$T_o = \begin{cases} F_{LF}(\theta, x_{\mathrm{CoM}})y_{LF}(\theta) + F_{RF}(\theta, x_{\mathrm{CoM}})y_{RF}(\theta)|_{\theta=\theta_b^*} = 0, \\ 0 \leqslant t < T/2 \\ F_{LR}(\theta, x_{\mathrm{CoM}})y_{LR}(\theta) + F_{RR}(\theta, x_{\mathrm{CoM}})y_{RR}(\theta)|_{\theta=\theta_b^*} = 0, \\ T/2 \leqslant t < T \end{cases} \qquad (17)$$

A sufficient condition for θ_b^* to satisfy Equation (17) arises when the two synchronized legs (LF, RF and LR, RR) that located on opposite sides of the CoM with equal distance (Equation (18)) select the same amount of obstacle disturbance forces (Equation (19)):

$$\begin{cases} y_{LF}(\theta) = -y_{RF}(\theta)|_{\theta=\theta_b^*} \\ y_{LR}(\theta) = -y_{RR}(\theta)|_{\theta=\theta_b^*} \end{cases} \qquad (18)$$

$$\begin{cases} F_{LF}(\theta, x_{\mathrm{CoM}}) = F_{RF}(\theta, x_{\mathrm{CoM}})|_{\theta=\theta_b^*} \\ F_{LR}(\theta, x_{\mathrm{CoM}}) = F_{RR}(\theta, x_{\mathrm{CoM}})|_{\theta=\theta_b^*} \end{cases} \qquad (19)$$

As discussed in Section 4.1, the ODF in the world frame for any contacting leg, F_i, is a fixed function of $\bar{x}_i$ (Equation (11)). Therefore, to satisfy Equation (19), the two synchronous legs should always contact the obstacles at the same relative position:

$$\begin{aligned} \bar{x}_{LF}(\theta, x_{\mathrm{CoM}}) &= \bar{x}_{RF}(\theta, x_{\mathrm{CoM}})|_{\theta=\theta_b^*} \\ \bar{x}_{LR}(\theta, x_{\mathrm{CoM}}) &= \bar{x}_{RR}(\theta, x_{\mathrm{CoM}})|_{\theta=\theta_b^*} \end{aligned} \qquad (20)$$

Therefore, if there exists a θ_b^* that satisfies Equation (20), then the resulting disturbance torques from a synchronized pair of legs will cancel each other out and result in a total of zero perturbation on the robot orientation, and such a θ_b^* would be an equilibrium orientation angle for the bounding gait. In Section 5.2 we discuss how this mechanism explains the equilibrium orientation observed from our experiment and simulation.

Obviously, another sufficient condition that satisfies Equation (17) would be

$$\begin{cases} F_{LF}(\theta, x_{\mathrm{CoM}}) = F_{RF}(\theta, x_{\mathrm{CoM}}) = 0|_{\theta=\theta_b^*} \\ F_{LR}(\theta, x_{\mathrm{CoM}}) = F_{RR}(\theta, x_{\mathrm{CoM}}) = 0|_{\theta=\theta_b^*} \end{cases} \qquad (21)$$

This condition corresponds to the trivial 90° equilibrium for bound.

5.1.2. Trotting analysis. For the trotting gait, the set of contacting legs S alternates between the two diagonal pairs of legs, LF, RR and RF, LR, and the equilibrium criterion in Equation (16) can be specified as

$$T_o = \begin{cases} F_{LF}(\theta, x_{\mathrm{CoM}})y_{LF}(\theta) + F_{RR}(\theta, x_{\mathrm{CoM}})y_{RR}(\theta)|_{\theta=\theta_t^*} = 0, \\ 0 \leqslant \mathrm{t} < \mathrm{T}/2 \\ F_{RF}(\theta, x_{\mathrm{CoM}})y_{RF}(\theta) + F_{LR}(\theta, x_{\mathrm{CoM}})y_{LR}(\theta)|_{\theta=\theta_t^*} = 0, \\ \mathrm{T}/2 \leqslant \mathrm{t} < \mathrm{T} \end{cases} \qquad (22)$$

A sufficient condition for θ_t^* to satisfy Equation (22) arises when the two synchronized legs (LF, RR and RF, LR) that located symmetrically on both sides of the CoM in lateral direction (Equation (23)) select the same amount of obstacle disturbance forces (Equation (24)):

$$\begin{cases} y_{LF}(\theta) = -y_{RR}(\theta)|_{\theta=\theta_t^*} \\ y_{RF}(\theta) = -y_{LR}(\theta)|_{\theta=\theta_t^*} \end{cases} \qquad (23)$$

$$\begin{cases} F_{LF}(\theta, x_{\mathrm{CoM}}) = F_{RR}(\theta, x_{\mathrm{CoM}})|_{\theta=\theta_t^*} \\ F_{RF}(\theta, x_{\mathrm{CoM}}) = F_{LR}(\theta, x_{\mathrm{CoM}})|_{\theta=\theta_t^*} \end{cases} \qquad (24)$$

and therefore cancel out the total torque on the CoM.

Using Equation (1) we can further simplify Equation (24) to the following:

$$\begin{aligned}\bar{x}_{LF}(\theta, x_{\mathrm{CoM}}) &= \bar{x}_{RR}(\theta, x_{\mathrm{CoM}})|_{\theta=\theta_t^*} \\ \bar{x}_{RF}(\theta, x_{\mathrm{CoM}}) &= \bar{x}_{LR}(\theta, x_{\mathrm{CoM}})|_{\theta=\theta_t^*}\end{aligned} \tag{25}$$

In Section 5.2 we demonstrate how to use this criterion to calculate the equilibrium orientation of trotting gait, θ_t^*, for different obstacle spacing and robot aspect ratio.

Similar to the bounding analysis, another sufficient condition that satisfies Equation (22) would be

$$\begin{cases} F_{LF}(\theta, x_{\mathrm{CoM}}) = F_{RR}(\theta, x_{\mathrm{CoM}}) = 0|_{\theta=\theta_t^*} \\ F_{RF}(\theta, x_{\mathrm{CoM}}) = F_{LR}(\theta, x_{\mathrm{CoM}}) = 0|_{\theta=\theta_t^*} \end{cases} \tag{26}$$

which corresponds to the trivial 90° equilibrium for trot.

5.2. Analytically calculating equilibrium orientations based on the steady-state mechanism

The derived equilibrium criteria (Equation (20) for bound, and Equation (25) for trot) in Section 5.1 provide a sufficient condition to maintain a steady-state orientation under repeated obstacle perturbation, which is to let the synchronously activated two legs always select the opposite obstacle disturbance torques. In this section, we show that this condition allows us to theoretically predict steady-state orientation positions observed from our experiments (Section 2) and simulation (Section 4.3) without numerical simulations.

In our experimental setup, the obstacle spatial distribution is periodic, and therefore the robot did not need to actively adapt its gait pattern to select the same $\bar{x}_i$ on the obstacle. Instead, with an appropriate orientation, θ^*, it would be able to maintain the same $\bar{x}_i$ for the synchronized pair of legs with a fixed gait, as long as θ^* satisfies the following conditions for the bounding gait:

$$\begin{aligned}x_{LF}(\theta, x_{\mathrm{CoM}}) - x_{RF}(\theta, x_{\mathrm{CoM}})|_{\theta=\theta_b^*} &= m(P+D) \\ x_{LR}(\theta, x_{\mathrm{CoM}}) - x_{RR}(\theta, x_{\mathrm{CoM}})|_{\theta=\theta_b^*} &= n(P+D)\end{aligned}$$

m and n are any constant integers. The condition for trotting gait are then

$$\begin{aligned}x_{LF}(\theta, x_{\mathrm{CoM}}) - x_{RR}(\theta, x_{\mathrm{CoM}})|_{\theta=\theta_t^*} &= m(P+D) \\ x_{RF}(\theta, x_{\mathrm{CoM}}) - x_{LR}(\theta, x_{\mathrm{CoM}})|_{\theta=\theta_t^*} &= n(P+D)\end{aligned}$$

These two equations provide the constraining conditions to calculate equilibrium orientation angles for periodic gaits like bounding and trotting. We interpret such constraints as solving a ''spatial period matching'' constraint.

The spatial period of a periodic robot gait, $T_{i,j}$, is defined as the x-direction distance between each synchronized pair of legs, $i, j \in H$:

$$T_{i,j} = x_i - x_j$$

For the bounding gait, there are two pairs of synchronized legs, LF, RF and LR, RR, and therefore the two spatial periods can be calculated from Equations (7)–(10):

$$\begin{cases} T_{LF,RF} = x_{LF} - x_{RF} = -2W\sin(\theta) \\ T_{LR,RR} = x_{LR} - x_{RR} = -2W\sin(\theta) \end{cases}$$

Similarly, for the trotting gait, the two spatial periods can be calculated as the x-direction distances of the pairs of synchronized legs, LF, RR and RF, LR:

$$\begin{cases} T_{LF,RR} = x_{LF} - x_{RR} = 2L\cos(\theta) - 2W\sin(\theta) \\ T_{RF,LR} = x_{RF} - x_{LR} = 2L\cos(\theta) + 2W\sin(\theta) \end{cases}$$

At θ^*, all robot spatial periods (e.g., $T_{LF,RF}$ and $T_{RF,RR}$ for a bounding gait, or $T_{LF,RR}$ and $T_{RF,LR}$ for a trotting gait) ''match'' the environment spatial period (i.e., spanning integer numbers of environmental spatial period $P+D$); the two synchronized legs are always contacting the obstacles at the same relative positions (Figures 8 and 9), and therefore exposed to the same amount of obstacle disturbance force, resulting in zero rotational perturbation and allowing the robot to maintain its current orientation, θ^*.

Therefore, the equilibrium orientation can be calculated by solving the spatial period matching constraints, which can be written for bounding as

$$\begin{aligned}T_{LF,RF}(\theta)|_{\theta=\theta_b^*} &= m(P+D) \\ T_{LR,RR}(\theta)|_{\theta=\theta_b^*} &= n(P+D)\end{aligned} \tag{27}$$

and for trotting as

$$\begin{aligned}T_{LF,RR}(\theta)|_{\theta=\theta_t^*} &= m(P+D) \\ T_{RF,LR}(\theta)|_{\theta=\theta_t^*} &= n(P+D)\end{aligned} \tag{28}$$

The leg–obstacle contact positions observed from both experiments (Figures 4 and 5, Extensions 1 and 2) and numerical simulation (Figure 10, Extensions 3 and 4) are qualitatively consistent with the criteria described by Equations (27) and (28).

The spatial period matching criterion enabled theoretical prediction of obstacle-modulated robot equilibrium states, and predictions of the dependence of the equilibrium angles on robot and environment parameters. Figure 11 shows the analytical prediction of equilibrium orientations for different obstacle spacings and robot aspect ratios. The model prediction agrees well with numerical simulation results and measurements from experiments.

Going forward, this stabilizing mechanism begins to suggest a novel gait control method to stabilize robot orientation under repeated obstacle collisions and disturbances. In Section 6, we discuss how multi-legged robots can use the ODS framework to actively adjust gait

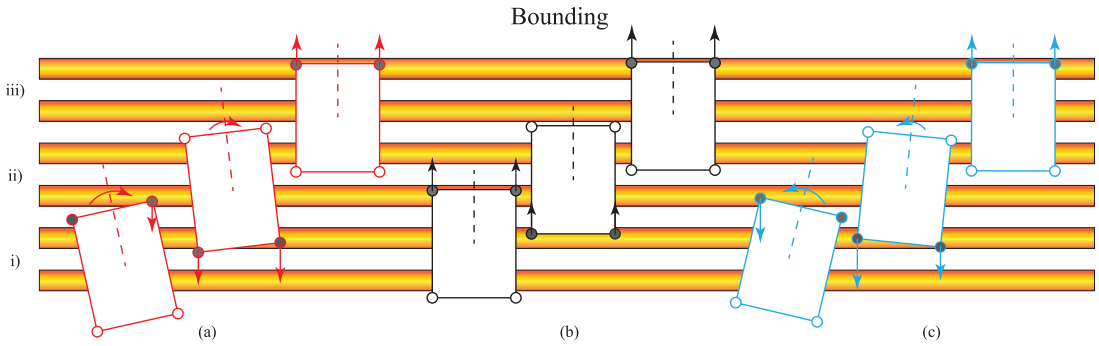

Fig. 8. Mechanism for a bounding robot to stabilize at 0° equilibrium orientation under repeated obstacle perturbation. (b) demonstrates the mechanism allowing a robot that starts at the equilibrium orientation θ^* to stay at θ^*. Since the two synchronous legs always select the same amount of obstacle disturbance force, the obstacle disturbance torques cancel each other out. (a) and (c) demonstrate an existing mechanism that allows a robot starting in the neighbourhood of the equilibrium to generate restoring torque towards the equilibrium orientation θ^*. i) Starting orientation of the robot. Solid circles represent activated pair of legs. Empty circles represent legs in the air. The length of straight arrows on solid circles represents qualitatively the amount of obstacle disturbance force (F_i, Figure 6C). Curved arrows represent the direction of total torque and resulting direction of robot yaw. ii) Subsequent orientation of the robot towards convergence to equilibrium orientation. iii) final orientation at the equilibrium θ^*. Marker conventions in (ii) and (iii) are the same as (i). Note that the lateral position of diagrams (i), (ii) and (iii) does not indicate the robot's direction of movement.

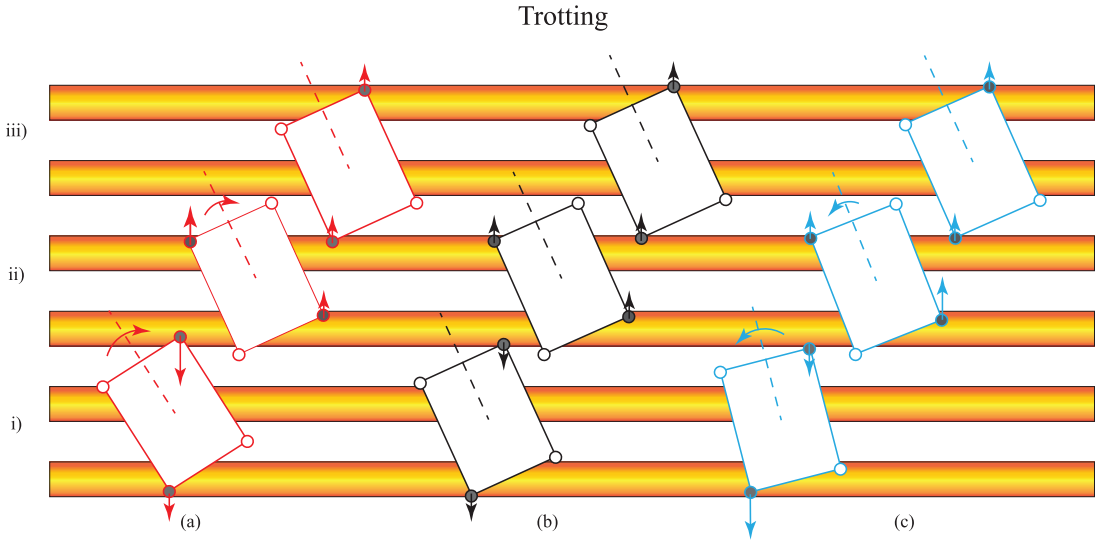

Fig. 9. Mechanism for a trotting robot to stabilize at 25° equilibrium orientation under repeated obstacle perturbation. (b) The mechanism allowing a robot that starts at the equilibrium orientation θ^* to stay at θ^*. Since the two synchronous legs always select the same amount of obstacle disturbance force, the obstacle disturbance torques cancel each other out. (a) and (c) An existing mechanism that allows a robot starting in the neighbourhood of the equilibrium to generate restoring torque towards the equilibrium orientation θ^*. (i) Starting orientation of the robot. Solid circles represent activated pair of legs. Empty circles represent legs in the air. The length of straight arrows on solid circles represents qualitatively the amount of obstacle disturbance force (F_i, Figure 6C). Curved arrows represent the direction of total torque and resulting direction of robot yaw. (ii) Subsequent orientation of the robot towards convergence to equilibrium orientation. (iii) Final orientation at the equilibrium θ^*. Marker conventions in (ii) and (iii) are the same as (i). Note that the lateral position of diagrams (i), (ii), and (iii) does not indicate the robot's direction of movement.

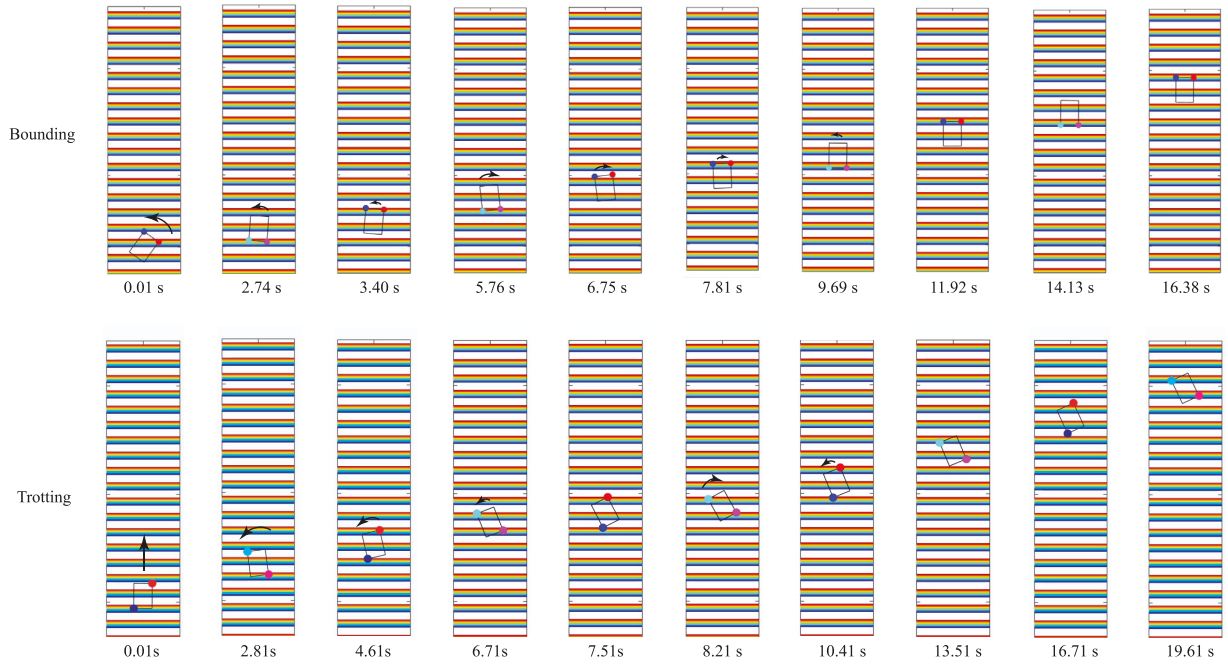

Fig. 10. Sequence of images from simulation showing a bounding robot's orientation locked to 0° under periodic obstacle modulation, whereas a trotting robot's orientation locked to -25° under the same obstacle modulation.

sequence to robustly move through randomly cluttered environments.

6. Broader applicability of the ODS framework

Section 5 reveals that the mechanism of the equilibrium robot orientation under repeated obstacle collisions is due to synchronized robot legs selecting cancelling obstacle disturbances and therefore neutralizing the total perturbation experienced by the CoM. For the structured environment studied in this article, periodic robot gaits passively generate such disturbance cancellation at the equilibrium orientations.

For non-structured environments, periodic gaits will no longer lead to equilibrium orientations. However, with the ODS representation (Section 3.1), a robot can plan a non-periodic gait to actively select cancelling obstacle disturbance torques and to reduce the perturbation in its orientation. Similarly, a robot might plan its gait to actively regulate total obstacle disturbance forces to maintain a constant speed.

In addition to stabilization, a robot can also use the ODS framework to actively exploit obstacle disturbances to achieve faster speed in translation or rotation. For example, to obtain a boost in the speed at each step, a robot might adjust the timing or position of obstacle interaction to always engage the obstacle on the negative

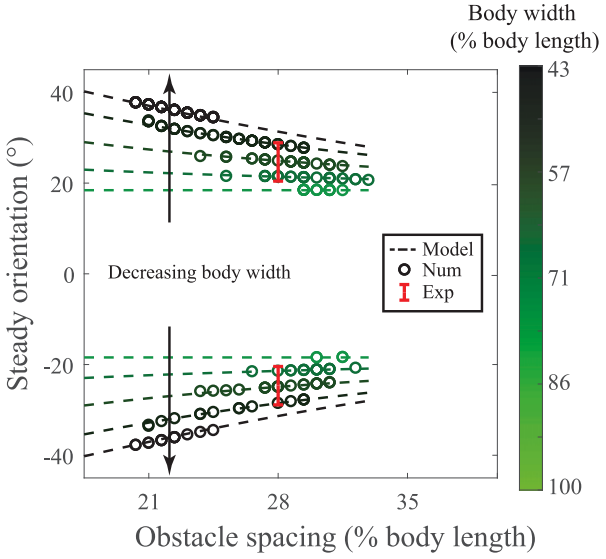

Fig. 11. Prediction of trotting robot equilibrium orientation angles as a function of log spacing for different robot aspect ratios. Red error bars represent average final orientation angles measured from trotting experiments (Figure 3C and D) with a robot body width of $2W = 25.4$cm ($\approx 71\%$ body length). Circles represent final orientations of equilibrium states computed from numerical simulation (Equations (14) and (15)). Dashed lines represent predictions using the spatial period matching constraints (by numerically solving Equations (27) and (28)). For simulation markers and model curves, color represents different robot half body widths (i.e., different aspect ratios).

(i.e., downhill) slopes. To exploit obstacles to turn clockwise, a robot can simply have all the right-hand side legs begin stance phase on positive (i.e., uphill) obstacle slopes and all the left-hand side legs begin stance phase on negative (i.e., downhill) slopes. Future work will investigate sensing options to implement these applications.

7. Conclusion

In this article, we propose a novel ODS framework that allows investigating and predicting robot dynamics under repeated obstacle disturbances. The ODS framework provides a novel representation of both physical environments and robot gait patterns, which allows systematic analysis of complex interactions between multi-legged platforms and obstacles, and suggests an approach to formal reasoning about how a locomotor could use the gait space affordances to actively exploit disturbances and collisions.

The ODS framework represents the cluttered environments as sources of obstacle disturbance force fields. This representation significantly simplifies the complexity of the contacts between high-DoF robot legs and high-DoF physical obstacles, and for the first time allow the assessment of opportunities for a robot to exploit its interaction with the environment as a source of locomotion affordances (Gibson, 1979) derived from locally-sensible physical properties such as shape and size.

The ODS framework represents robot legs or body segments as a collection of ''disturbance force selectors'' leveraged to adjust actual total environment perturbation that affects CoM dynamics. With sufficient knowledge of the environment, we envision that a multi-legged robot can use the ODF framework to adjust the timing or contact position of leg–obstacle interactions to actively select available disturbances and generate desired interaction dynamics for an ''obstacle-aided'' locomotion and navigation in cluttered environments.

We note that this study is the first step towards a more complete connection between gait space and environment affordances. Future work such as extension of the horizontal-plane model to three dimensions, and further investigation of coupling between non-periodic gaits with less-structured environments, will allow creation of more general and complete versions of the disturbance selection framework. We envision such development will aid control and planning strategies for future robots to move through complex environments.

Acknowledgements

We thank Christopher Zawacki for his assistance in designing the robot platform. We thank Zhichao Liu and Divya Ramesh for their assistance in preliminary data collection.

Funding

The author(s) disclosed receipt of the following financial support for the research, authorship, and/or publication of this article: This research was supported by the National Science Foundation (NSF) under an INSPIRE award (number CISE NRI 1514882) and NRI INT award (number 1734355).

Notes

1. In this article we are mainly concerned about the horizontal plane dynamics and robot yaw angles, and we refer to pitch and roll in a colloquial sense without a rigorous definition.
2. The mechanism and dynamics of the limit cycles are beyond the scope of this article and are therefore only included here for observation completeness and will not be discussed further in the rest of the article. Here we qualitatively use the term limit cycle behavior to refer the periodic oscillation observed in the horizontal-plane CoM trajectories.
3. Here $\mathcal{P}$ denotes the powerset.
4. Simulation data suggested that obstacle-modulated robot steady states were insensitive to small variations in function forms used to represent the SLSO ODF. Future work should systematically investigate the exact form.
5. Here $mod(A, B)$ denotes the fractional portion of A/B.
6. As a result, the model only calculates the orientation but not the translational direction of the robot.
7. This threshold was arbitrarily selected as an epsilon value to serve as the a qualitative estimation of the noise floor.

ORCID iD

Feifei Qian https://orcid.org/0000-0001-9656-1168

References

ArslanÖ and Saranli U (2012) Reactive planning and control of planar spring–mass running on rough terrain. *IEEE Transactions on Robotics* 28(3): 567–579.

Bayraktaroglu ZY and Blazevic P (2005) Understanding snakelike locomotion through a novel push-point approach. *Journal of Dynamic Systems, Measurement, and Control* 127(1): 146–152.

Blickhan R (1989) The spring-mass model for running and hopping. *Journal of Biomechanics* 22(11-12): 1217–1227.

Brown IE and Loeb GE (2000) A reductionist approach to creating and using neuromusculoskeletal models. In: *Biomechanics and neural control of posture and movement*. Berlin: Springer, pp. 148–163.

Byl K and Tedrake R (2009) Metastable walking machines. *The International Journal of Robotics Research* 28(8): 1040–1064.

Curet OM, Patankar NA, Lauder GV and MacIver MA (2010) Aquatic manoeuvering with counter-propagating waves: a novel locomotive strategy. *Journal of The Royal Society Interface* 8(60): 1041–1050.

De A and Koditschek DE (2018) Vertical hopper compositions for preflexive and feedback-stabilized quadrupedal bounding, pacing, pronking, and trotting. *The International Journal of Robotics Research* 37(7): 743–778.

Full RJ and Koditschek DE (1999) Templates and anchors: Neuromechanical hypotheses of legged locomotion on land. *Journal of experimental biology* 202(23): 3325–3332.

Gart SW and Li C (2018) Body-terrain interaction affects large bump traversal of insects and legged robots. *Bioinspiration and Biomimetics* 13(2): 026005.

Gart SW, Mitchel TW and Li C (2019) Snakes partition their body to traverse large steps stably. *Journal of Experimental Biology* 222(8): jeb185991.

Gart SW, Yan C, Othayoth R, Ren Z and Li C (2018) Dynamic traversal of large gaps by insects and legged robots reveals a template. *Bioinspiration and Biomimetics* 13(2): 026006.

Gibson J (1979) *The theory of affordances the ecological approach to visual perception*. Boston, MA: Houghton Mifflin, pp. 127–143.

Johnson AM and Koditschek D (2013) Toward a vocabulary of legged leaping. Technical report, University of Pennsylvania.

Kenneally GD, De A and Koditschek DE (2016) Design principles for a family of direct-drive legged robots. *IEEE Robotics and Automation Letters* 1(2): 900–907.

Khatib O (1986) Real-time obstacle avoidance for manipulators and mobile robots. In: *Autonomous robot vehicles*. Berlin: Springer, pp. 396–404.

Kim S, Spenko M, Trujillo S, Heyneman B, Santos D and Cutkosky MR (2008) Smooth vertical surface climbing with directional adhesion. *IEEE Transactions on robotics* 24(1): 65–74.

Kinsey CT and McBrayer LD (2018) Forelimb position affects facultative bipedal locomotion in lizards. *Journal of Experimental Biology* 221(24): jeb185975.

Kohlsdorf T and Biewener A (2006) Negotiating obstacles: running kinematics of the lizard sceloporus malachiticus. *Journal of Zoology* 270(2): 359–371.

LaValle SM (2006) *Planning algorithms*. Cambridge: Cambridge University Press.

Li C, Pullin AO, Haldane DW, Lam HK, Fearing RS and Full RJ (2015) Terradynamically streamlined shapes in animals and robots enhance traversability through densely cluttered terrain. *Bioinspiration and Biomimetics* 10(4): 046003.

Li C, Umbanhowar PB, Komsuoglu H and Goldman DI (2010) The effect of limb kinematics on the speed of a legged robot on granular media. *Experimental mechanics* 50(9): 1383–1393.

Marvi H, Gong C, Gravish N, et al. (2014) Sidewinding with minimal slip: Snake and robot ascent of sandy slopes. *Science* 346(6206): 224–229.

McInroe B, Astley HC, Gong C, et al. (2016) Tail use improves performance on soft substrates in models of early vertebrate land locomotors. *Science* 353(6295): 154–158.

Qian F and Goldman DI (2015a) Anticipatory control using substrate manipulation enables trajectory control of legged locomotion on heterogeneous granular media. In: *Micro-and Nanotechnology Sensors, Systems, and Applications VII (Proceedings of SPIE*, Vol. 9467). International Society for Optics and Photonics, 94671U.

Qian F and Goldman DI (2015b) The dynamics of legged locomotion in heterogeneous terrain: universality in scattering and sensitivity to initial conditions. In: *Robotics: Science and Systems*.

Qian F, Zhang T, Li C, et al. (2013) Walking and running on yielding and fluidizing ground. In: *Robotics: Science and Systems*.

Raibert MH (1986) *Legged robots that balance*. Cambridge, MA: MIT Press.

Rieser JM, Schiebel PE, Pazouki A, et al. (2019) Dynamics of scattering in undulatory active collisions. *Physical Review E* 99(2): 022606.

Sane SP and Dickinson MH (2001) The control of flight force by a flapping wing: lift and drag production. *Journal of Experimental Biology* 204(15): 2607–2626.

Saranli U, Buehler M and Koditschek DE (2001) Rhex: A simple and highly mobile hexapod robot. *The International Journal of Robotics Research* 20(7): 616–631.

Schiebel PE, Rieser JM, Hubbard AM, Chen L, Rocklin DZ and Goldman DI (2019) Mechanical diffraction reveals the role of passive dynamics in a slithering snake. *Proceedings of the National Academy of Sciences* 116(11): 4798–4803.

Schmitt J and Holmes P (2000) Mechanical models for insect locomotion: dynamics and stability in the horizontal plane I. Theory. *Biological Cybernetics* 83(6): 501–515.

Transeth AA, Leine RI, Glocker C, Pettersen KY and Liljebäck P (2008) Snake robot obstacle-aided locomotion: Modeling, simulations, and experiments. *IEEE Transactions on Robotics* 24(1): 88–104.

Wilshin S, Reeve MA, Haynes GC, Revzen S, Koditschek DE and Spence AJ (2017) Longitudinal quasi-static stability predicts changes in dog gait on rough terrain. *Journal of Experimental Biology* 220(10): 1864–1874.

Winter AG, Deits RL, Dorsch DS, Slocum AH and Hosoi AE (2014) Razor clam to RoboClam: Burrowing drag reduction mechanisms and their robotic adaptation. *Bioinspiration and Biomimetics* 9(3): 036009.

Winter AG, Deits RL and Hosoi AE (2012) Localized fluidization burrowing mechanics of *Ensis directus*. *Journal of Experimental Biology* 215(12): 2072–2080.

Zhong B, Aydin YO, Gong C, et al. (2018) Coordination of back bending and leg movements for quadrupedal locomotion. In: *Robotics: Science and Systems*.

Appendix A. Index to multimedia extensions

Archives of IJRR multimedia extensions published prior to 2014 can be found at http://www.ijrr.org, after 2014 all videos are available on the IJRR YouTube channel at http://www.youtube.com/user/ijrrmultimedia

Table of Multimedia Extensions

Extension	Media type	Description
1	Video	Experimental bounding gait
2	Video	Experimental trotting gait
3	Video	Simulation bounding gait
4	Video	Simulation trotting gait

Appendix B. List of symbols

L	Robot half body length
W	Robot half body width
P	Obstacle spacing
D	Obstacle diameter
β	Surface inclination angle
m	Mass of the robot
I	Moment of inertia of the robot
q	Robot CoM state on horizontal plane
θ	Robot orientation
x_{CoM}	Position of robot CoM along the x axis (fore–aft direction in the world frame)
y_{CoM}	Position of robot CoM along the y axis (lateral direction in the world frame)
x_i	Position of leg i along the x axis (fore–aft direction in the world frame)
y_i	Position of leg i along the y axis (lateral direction in the world frame)
H	Set of all legs
S	Set of contacting legs
T	Stride period
O	Region on the horizontal plane that is occupied by obstacles
G	Region on the horizontal plane that is not occupied by obstacles
$T_{i,j}$	Spatial period of a periodic gait
$\bar{x}$	Relative contact position on the obstacle
f	Obstacle disturbance force from a single obstacle
F_i	Obstacle disturbance force field
F_o	Total obstacle disturbance force on robot CoM
F_{th}	Thrust force
F_d	Damping force
c_F	Thrust force constant
c_x	Linear damping coefficient
T_d	Damping torque
c_θ	Angular damping coefficient
T_o	Total obstacle disturbance torque on robot CoM